9

Alternative Reconstruction Method and Object Analysis in Digital Holographic Microscopy

Francisco Palacios et al *
University of Oriente
Cuba

1. Introduction

Holography is a method for storing and reconstructing both amplitude and phase information of a wave front. In digital holography the reconstruction process is accomplished by means of a computer (Yaroslavsky & Merzyalov, 1980) obtaining directly the phase distribution of the object wave front. Particularly with the improvement of the spatial resolution of CCD cameras and the increasing computational performance of personal computers digital holography has been widely applied in many fields such as deformation analysis (Schedin et al., 2001), object contouring (Wagner et al., 2000), microscopy (Takaki & Ohzu, 1999) and particle measurement (Murata & Yasuda, 2000). The technique of digital holography has been implemented in a configuration of an optical microscope (Schilling et al., 1997); the objective lens produces a magnified image of the object and the interference between this image and the reference beam is achieved by the integration of the microscope into one of the arms of a Mach-Zender interferometer. This configuration is called Digital Holographic Microscopy (DHM).

DHM is a powerful technique for real-time quantitative phase contrast imaging, since a single intensity image, called a hologram, allows the reconstruction of the phase shift induced by a specimen. This property of holograms offers phase-contrast techniques, which can then be used for quantitative 3D imaging (Palacios et al., 2005). Quantitative phase imaging is important because it allows the determination of the optical thickness profile of a transparent object with sub-wavelength accuracy (Yu et al., 2009). Through numerical processing of the hologram one can filter out parasitic interferences and the components of the image reconstruction: zero-order and twin image terms (Cuche et al., 2000) or to compensate for curvature introduced by the microscope objective (MO) (Pedrini et al., 2001),

* Oneida Font[1], Jorge Ricardo[1], Guillermo Palacios[1], Mikiya Muramatsu[2], Diogo Soga[2], Daniel Palacios[3], José Valin[4] and Freddy Monroy[5]
[1]*University of Oriente, Cuba*
[2]*University of Sao Paulo, Brasil*
[3]*University of Simon Bolivar, Venezuela*
[4]*Polytechnic Institute "José A. Echeverría", Cuba*
[5]*National University of Colombia, Colombia*

spherical aberration (Stadelmaier & Massig, 2000), astigmatism (Grilli et al., 2001) and anamorphism (De Nicola et al., 2005).

Compensation of aberrations is fundamental when quantitative phase determination is used in microscopic metrological applications. Several approaches have been proposed to remove the aberrations. A method proposed by Cuche (Cuche et al., 1999) used a single hologram, which involved the computation of a digital replica of the reference wave depending on two reconstruction parameters. A double-exposure technique (Ferraro et al., 2003) can compensate completely the inherent wave front curvature in quantitative phase contrast imaging, although it needs two hologram recordings with and without the sample and a subtraction procedure between the two holograms. In the paper (Colomb et al., 2006) the authors developed a method to compensate the tilt aberration by recording a hologram corresponding to a blank image to compute the first-order parameters directly from the hologram. However, the method is limited to selecting profiles or areas known to be flat in the hologram plane. A method was proposed by Miccio (Miccio et al., 2007) who performed a two-dimensional fitting with the Zernike polynomials of the reconstructed unwrapped phase, although the application of the method is limited to be the special case of thin objects.

For image reconstruction different algorithms have been developed. Among them, the Single Fourier Transform Formulation (SFTF) (Schnars, 1994), the convolution-based algorithm (CV) (Demetrakopoulos & Mittra, 1974) and the angular spectrum-based algorithm (ASA) (Yu & Kim, 2005) are most commonly used. The SFTF algorithm is fast and can be used with objects larger than a CCD. However, variation of the size of the reconstructed image as result of a change in the reconstruction depth poses problems in applications such as reconstruction of color holograms (Yamaguchi et al., 2002) and particle sizing (Pan & Meng, 2003). In contrast, the CV algorithm keeps the size of the reconstructed image the same as that of the CCD. However, it is applicable only to objects that are smaller than the CCD. In addition, when the CV algorithm is used for objects much smaller than a CCD, it degrades the image quality, since the image is represented by only a small number of pixels. The CV algorithm was extended to large objects by zero padding the holograms before reconstruction (Kreis et al., 1997). This approach, however, led to an increase in computational load.

To avoid a number of limitations of the previous algorithms, the double Fresnel-transform algorithm (DBFT) that allows the reconstruction of digital holograms with adjustable magnification was developed (Zhang et al., 2004). This algorithm involves two reconstruction steps implemented by a conventional single Fourier-transform algorithm. Through the adjustment of the distance parameter in the first stages, it is possible to control the size of the reconstructed images, independent of distance and wavelength, even for objects larger than a CCD without any computational penalty.

The method of image reconstruction proposed here is similar to the DBFT algorithm, since we also use two steps for image reconstruction, but they differ in the objectives and meaning of the two steps. Our formulation is specific for digital holographic microscopy; this way the objective of the first stage is the calculation of the objects' Fourier transform plane, where the complex wavefield contains all the information about the phase and intensity of object wavefield. Then, the second step is to reconstruct the complex amplitudes of the image wavefield starting from the objects' Fourier transform plane. We will describe and show advantages of the proposed method.

2. Experimental set-up

Figure 1 shows the experimental set-up used in this work. It is a Digital Holographic Microscope designed for transmission imaging with transparent sample. The basic architecture is that of a Mach-Zehnder interferometer. A linearly polarized He-Ne laser (15 mW) is used as light source. The expanded beam from the laser is divided by the beam splitter BS1 into reference and object beams. The microscope produces a magnified image of the object and the hologram plane is located between the microscope objective MO and the image plane *(x′-y′)* which is at a distance *d′* from the recording hologram plane *(ξ-η)*. In digital holographic microscopy we can consider the object wave emerging from the magnified image and not from the object itself (VanLigten & Osterberg, 1966).

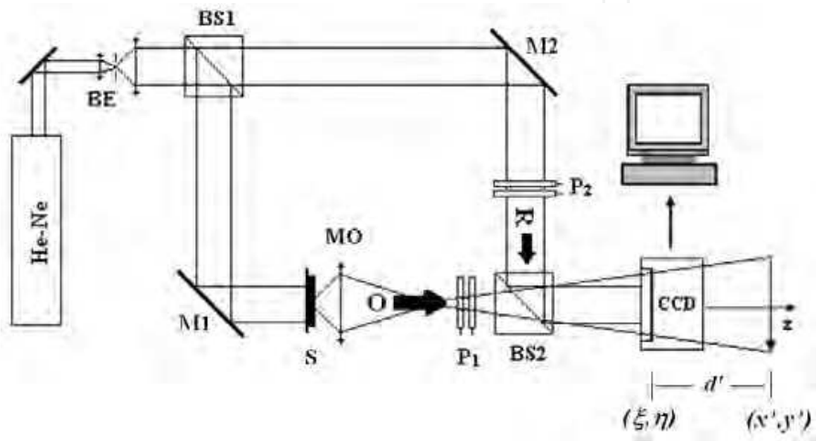

Fig. 1. Experimental set-up: BE, bean expander; BS, bean splitter (the splitting ratio of BS1 and BS2 are 90/10 and 50/50 respectively); M, mirror; MO, microscope objective; S, sample; P, dual polarizer; CCD, charge coupled device.

With the combinations of the dual polarizer $\boldsymbol{P_1}$ and $\boldsymbol{P_2}$ the intensities are adjusted in the reference arm and the object arm of the interferometer and the same polarization state is also guaranteed for both arms improving their interference. The specimen S is illuminated by a plane wave and a microscope objective, that produces a wave front called object wave *O*, collects the transmitted light**.** A condenser, not shown, is used to concentrate the light or focus the light in order that the entire beam passes into the MO. At the exit of the interferometer the two beams are combined by beam splitter BS2 being formed at the CCD plane the interference pattern between the object wave *O* and the reference wave *R*, which is recorded as the hologram of intensity $I_H(\xi,\eta)$,

$$I_H(\xi,\eta) = |O|^2 + |R|^2 + R^*O + RO^* \tag{1}$$

where R^* and O^* are the complex conjugates of the reference and object waves, respectively. The two first terms form the zero-order, the third and fourth terms are respectively the virtual (or conjugate image) and real image, which correspond to the interference terms. The off-axis geometry is considered; for this reason the mirror M2, which reflects the reference wave, is oriented so that the reference wave reaches the CCD camera with a small incidence angle with respect to the propagation direction of the object wave. A digital hologram is recorded by the CCD camera HDCE-10 with 1024x768 square pixels of size 4.65 μm, and

transmitted to the computer by means of the IEEE 1394 interface. The digital hologram $I_H(j,l)$ is an array of $M \times N = 1024 \times 768$ 8-bit-encoded numbers that results from the two-dimensional sampling of $I_H(\xi,\eta)$ by the CCD camera,

$$I_H(j,l) = I_H(\xi,\eta)\,\mathrm{rect}\left[\frac{\xi}{L_x},\frac{\eta}{L_y}\right]\sum_{j=-M/2}^{M/2}\sum_{l=-N/2}^{N/2}\delta(\xi - j\Delta\xi, \eta - l\Delta\eta) \tag{2}$$

where j, l are integers defining the positions of the hologram pixels and $\Delta\xi = \Delta\eta = 4.65\ \mu m$ defines the sampling intervals in the hologram plane.

3. Basic principles of the alternative reconstruction method

In Digital Holographic Microscopy the field produced by the objective lens can be reconstructed in any plane along the field propagation direction. Traditionally the optical field $\psi(x',y')$ on the image plane $(x'\text{-}y')$ is calculated by propagation of the wavefront $\psi(\xi,\eta)$, a distance $z = d'$ from the hologram plane $(\xi\text{-}\eta)$, figure 2.

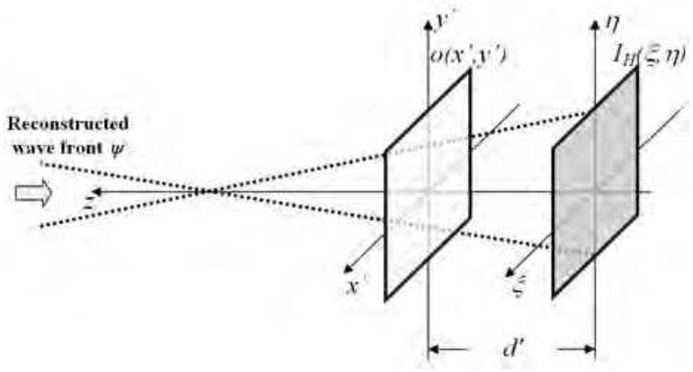

Fig. 2. Schematic diagram of traditional image reconstruction methods in DHM.

In our approach the reconstruction of the complex wave distribution $o(x',y') \equiv \psi(x',y';z=d')$ consists basically of two stages that involve two wavefield propagations. In the first stage, figure 3, we reconstruct the wave distribution $\tilde{o}(u,v)$ on the $(u\text{-}v)$ plane at reconstruction distance z = D (first propagation).

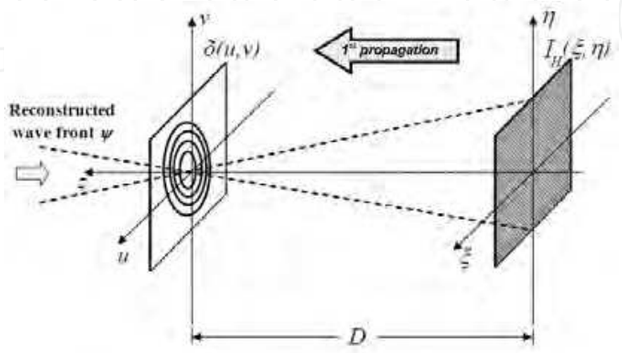

Fig. 3. Reconstruction of the wave distribution $\tilde{o}(u,v)$ on the $(u\text{-}v)$ plane at reconstruction distance z = D (first propagation).

Applying the (ASA) algorithm the distance D is calculated, as shown in section 3.1.1**.** After the distance D has been calculated, the first propagation is carried out by means of the Fresnel approximation method, specifically the S*ingle* F*ourier* T*ransform* F*ormulation* (SFTF),

$$\psi_{SFTF}(u,v;z) = A\exp\left[\frac{i\pi}{\lambda z}\left(u^2+v^2\right)\right]\Im\left\{I_H(\xi,\eta)\exp\left[\frac{i\pi}{\lambda z}\left(\xi^2+\eta^2\right)\right]\right\} \tag{3}$$

where z is the reconstruction distance, $\Im$ is an operator that denotes the Fourier transform, $A=exp(i2\pi z/\lambda)/(i\pi\lambda)$ and considering a plane reference wave with unit strength perpendicular to the recording plane.

At z = D, the reconstructed wavefield, consists of a zero order and the twin images (real and conjugate). The filtered complex wavefield $\psi^f_{SFTF}(u,v;z=D)$ can be expressed by Eq. (4) by replacing the specimen hologram $I_H(\xi,\eta)$ with a filtered hologram $I^f_H(\xi,\eta)=RO^*$ containing only spatial components of the real image (Cuche et al., 2000),

$$\psi^f_{SFTF}(u,v;z=D) = A\exp\left[\frac{i\pi}{\lambda D}\left(u^2+v^2\right)\right]\Im\left\{I^f_H(\xi,\eta)\exp\left[\frac{i\pi}{\lambda D}\left(\xi^2+\eta^2\right)\right]\right\} \tag{4}$$

As has been proven (Palacios et al., 2008), the complex field $\psi^f_{SFTF}(u,v;z=D)$ is equivalent to the complex field distribution $\tilde{o}(u,v)$ on the back focal plane of the objective lens. From Abbe's theory of image formation (Lipson S. & Lipson H., 1981), the field on the back focal plane can be represented by the expression,

$$\psi^f_{SFTF}(u,v;z=D) \cong \tilde{o}(u,v) = S_\phi(u,v)\Im\left[o(x_o,y_o,\lambda f)\right] \tag{5}$$

where $\Im\{o(x_o, y_o, \lambda f)\}$ is the Fourier transform of the object wave distribution at the plane $(u-v)$, with $o(x_o,y_o)$, the amplitude transmittance of the object,

$$\Im\left[o(x_o,y_o,\lambda f)\right] = \iint o(x_o,y_o)\exp\left[-i\frac{2\pi}{\lambda f}(x_o u + y_o v)\right]dx_o dy_o \tag{6}$$

and $S_\phi(u,v)$ is a quadratic phase factor,

$$S_\phi(u,v) = \frac{i}{\lambda f}\exp\left[-ik(S_o+f)\right]\exp\left[\frac{ik}{2f}\left(u^2+v^2\right)\left(1-\frac{S_o}{f}\right)\right] \tag{7}$$

where S_o is the distance from the object to the lens, f the focal distance of the lens, λ the wavelength of the incident plane wave.

From the wave theory of image formation, after the objective lens producing the diffraction pattern of the object in its back focal plane, a second Fourier transformation performed on the diffraction pattern it is associated with the image of the object (Goodman, 1968). Consequently, all the information about image wavefield at the hologram plane is contained in the complex wavefront $o(u,v)$ on the back focal plane, therefore the reconstruction of the optical wavefield $o(x',y';d')$ can be carried out from the $(u-v)$ plane, instead of traditionally the hologram plane $(\xi-\eta)$, figure 4.

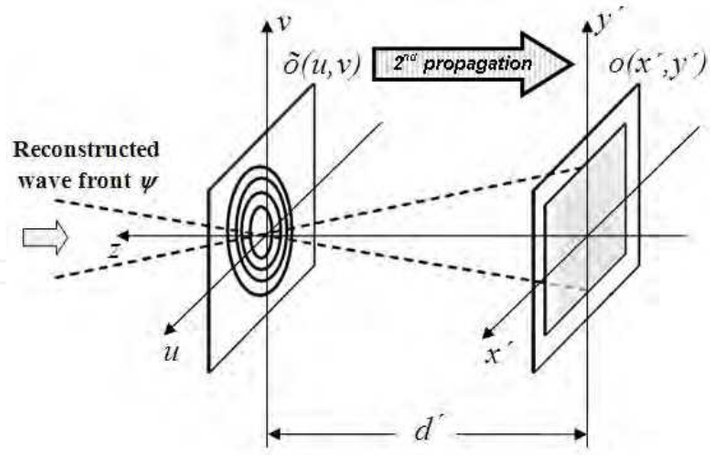

Fig. 4. Reconstruction of the optical wavefield $o(x',y';d')$ in the image plane from the $(u\text{-}v)$ plane (second propagation).

In the second stage of the method, the complex wavefield $\psi(x',y';d')$ at an arbitrary distance d' can be obtained by propagation of the wavefield $\tilde{o}(u,v)$ through a distance d' and the result is inverse Fourier transformed,

$$\psi(x',y';d') = \Im^{-1}\left[\psi^{f}_{SFTF}(u,v;z=D)\exp\left(i\,d'\sqrt{k^2+k_u^2+k_v^2}\right)\right] \tag{8}$$

where $\Im^{-1}$ symbolizes the inverse Fourier Transform, $k=2\pi/\lambda$, k_u and k_v are corresponding spatial frequencies of u and v respectively. The numerical implementation of Eq. (8), that we call the D*ouble*-P*ropagation* algorithm (DPA), is given by,

$$\begin{aligned}\psi_{DPA}(m,n;d') = FFT^{-1}\Big\{ & \psi^{f}_{SFTF}(l,j;z=D) \\ & \times\exp\left[2\pi i\,d'\sqrt{(1/\lambda)^2+(l/N\Delta\xi)^2+(j/M\Delta\eta)^2}\right]\Big\}\end{aligned} \tag{9}$$

where j, l, m, n are integers $(-M/2 < j, l < M/2)$, $(-N/2 < m, n < N/2)$ and $\psi^{f}_{SFTF}(l,j;z=D)$ is the discrete formulation of Eq. (4). From Eq. (9) we can obtain the intensity image $I_{DPA}(x',y';d')$ by calculating $|\psi_{DPA}(m,n;d')|^2$ and the phase image $\phi_{DPA}(x',y';d')$ by calculating $\arg[\psi_{DPA}(m,n;d')]$.

In short, the following steps describe the general procedure of the alternative reconstruction method:

1. Determining the distance D.
2. Calculate $\psi_{SFTF}(u,v;z=D)$ using Eq. (3), i.e., the complex amplitudes of the wavefield at $z=D$.
3. Obtaining $\psi^{f}_{SFTF}(u,v;z=D)$ by filtering the spatial components that correspond to the complex amplitudes of the Fourier transform of the objects.
4. Calculate $\psi_{DPA}(m,n;d')$, using Eq. (9), at an arbitrary distance d'.
5. Determining the intensity image or the phase image by calculating the square modulus or the argument of Eq. (9).

As we will demonstrate in next section, the formulation based on Eq. (9) guarantees that the reconstructed image maintains its size independently of depth d' and the phase curvature compensation can be done easily by techniques of image background subtraction**.**

3.1 Experimental validation of the method: advantages and limitations

Figure 5(a) shows the hologram of a USAF resolution target recorded by the experimental set-up. In figure 5(b) are represented the components of the reconstructed wavefields at $z = D$. The undiffracted reconstruction wave forms a zero-order image which is located in the center (already filtered), and corresponds to the first two terms on the right-hand side of Eq. (1).

Due to off-axis geometry the real image (delimited by the circle) and the conjugate image (delimited by the rectangle) are positioned at different locations on the reconstruction plane and they correspond to the interference terms on the right-hand side of Eq. (1). The separation of the interference terms depends on the angle between the reference and object wave. In figure 5b the expression $log[1+|(\psi_{SFTF}(x'y',d'= D)|^2]$ was used to compress the dynamic range of pixel values, which improves the visualization of the intensity distribution of the reconstructed wavefields (Lim, 1990).

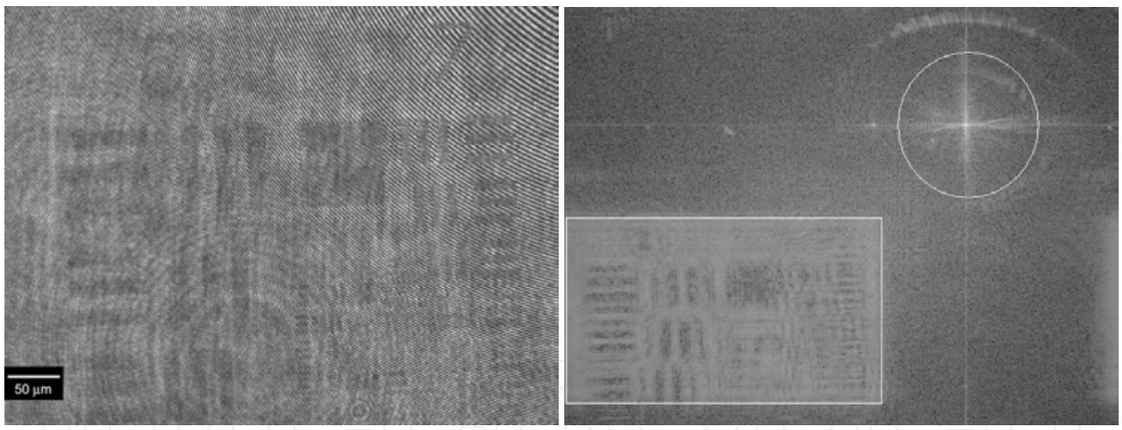

(a) (b)

Fig. 5. (a) Hologram of a USAF resolution target, (b) Components of the reconstructed wavefield at $z = D$. The circle delimits the real image and the rectangle the conjugate image.

At $z = D$ the reconstruction of real image is different of the genuine appearance of object image because at this distance the Fraunhofer diffraction pattern of the objects is reconstructed, figure 6, rather than the image of the objects.

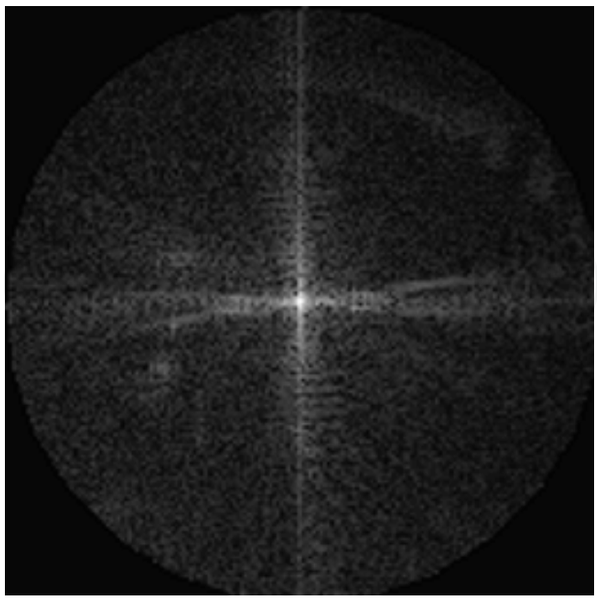

Fig. 6. Intensity of field distribution on the focal plane.

Larger or lower spatial frequencies of object decomposition will be represented by intensity in the focal plane that is farther or closer from optical axis or equivalently farther or closer from the center of the pattern where is contained the undiffracted object wavefield.

3.1.1 Determination of the distance *D*

The distance D is determined only one time, and remains the same until there is some variation in the experimental set-up. Applying the (ASA) algorithm, the following steps were performed to calculate the distance D:

1. The angular spectrum $A(k_\xi k_\eta;z=0)$ of the hologram $I_H(\xi,\eta)$ at $z = 0$ is obtained by taking its Fourier transform. $k_\xi$and k_η are the corresponding spatial frequencies in the hologram plane ξ-η.
2. Filtering of the angular spectrum to suppress both the zero-order and the twin image. In this step a region of interest corresponding only to the object spectrum is selected and the modified angular spectrum $\tilde{A}_H\left(k_\xi,k_\eta;z=0\right)$ is obtained.
3. The new angular spectrum at plane z, $A(k_\xi k_\eta;z)$ is calculated from $\tilde{A}_H\left(k_\xi,k_\eta;0\right)$ as, $A\left(k_\xi,k_\eta;z\right)=\tilde{A}\left(k_\xi,k_\eta;0\right)\exp\left[ik_z z\right]$, where $k_z=\sqrt{k^2-k_\xi^2-k_\eta^2}$.
4. The reconstructed complex wave field at any plane $(x'\text{-}y')$ perpendicular to the propagating z axis is found by,
   $$\psi_{ASA}\left(x',y';z\right)=\iint A\left(k_\xi,k_\eta;z\right)\exp\left[\,i\left(k_\xi x'+k_\eta x'\right)\right]dk_\xi\,dk_\eta\ .$$
5. The reconstruction of the amplitude image $I_{ASA}(x',y';z)=|\,\Psi_{ASA}(x',y';z)\,|^2$, is carried out varying z from 0 to $300\ mm$ with $20\ mm$ as incremental step. The punctual maximum value $P(z) = [I_{ASA}(x',y';z)]_{max}$ is calculated and plotted for each z, figure 7.
6. Between the two points around the relative maximum the incremental step is reduced to $1\ mm$. The distance D is equal to the z value at which the absolute maximum of $I_{ASA}(x',y';z)_{max}$ is reached; the value of $z = D = 173\ mm$ is shows in figure 7.

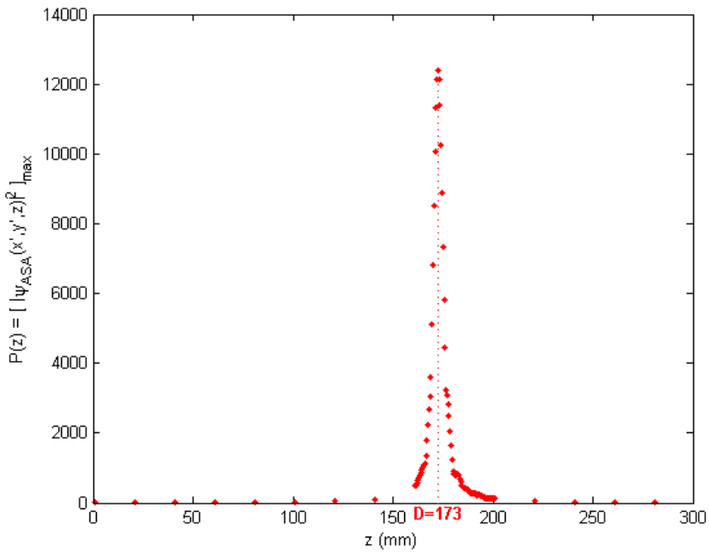

Fig. 7. Distance D determination using *ASA*.

Because the reference wave is plane, the distance D is the physical distance from the hologram to back focal point of the objective lens.

3.1.2 Behavior of the wavefield near to the back focal plane

Using the hologram of figure 5a, the behavior of the wavefield near the back focal plane is visualized. With *z* ranging from *141 mm* to *173 mm* and incremental step of *8 mm* a sequence of image reconstructions is presented in figure 8. The sequence shows the change of phase (A) and intensity (B) calculated from the expressions: $\arg(FFT^{-1}[\psi_{SFTF}(l,j;z)])$ and $log[1+|(\psi_{SFTF}(l,j;z)|^2]$ respectively.

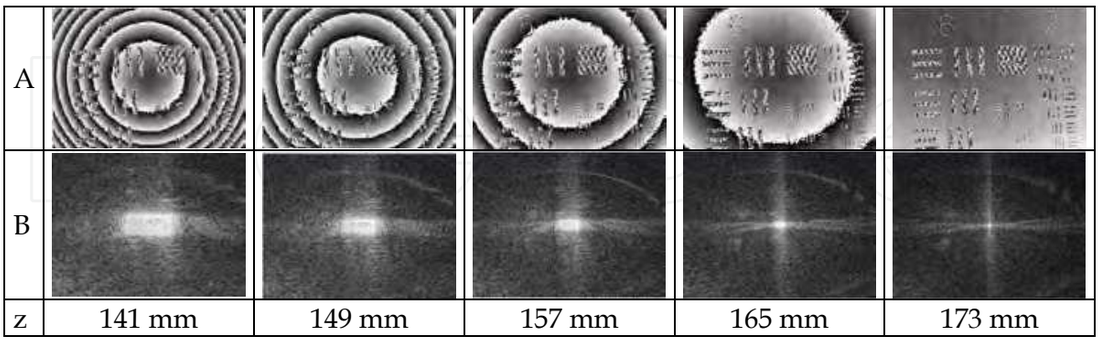

Fig. 8. Behavior of the wavefield in the region of the back focal plane.

From figure 8 it is corroborated that as the reconstruction plane approaches the focal plane, the phase jumps between the reference and object waves gradually disappear. These phase jumps totally disappear for z = *D* = *173 mm*, where the focal plane is reconstructed. This behaviour allows us to conclude that the curvature of the wavefront has a minimum on the focal plane and it is increased as the wavefield propagates away from this plane.

3.1.3 Intensity and phase image reconstruction

Calculating the square modulus and the argument of Eq. (9) in figure 9 provide the intensity (a) and phase (b) image reconstruction respectively at $z = D = 173\ mm$.

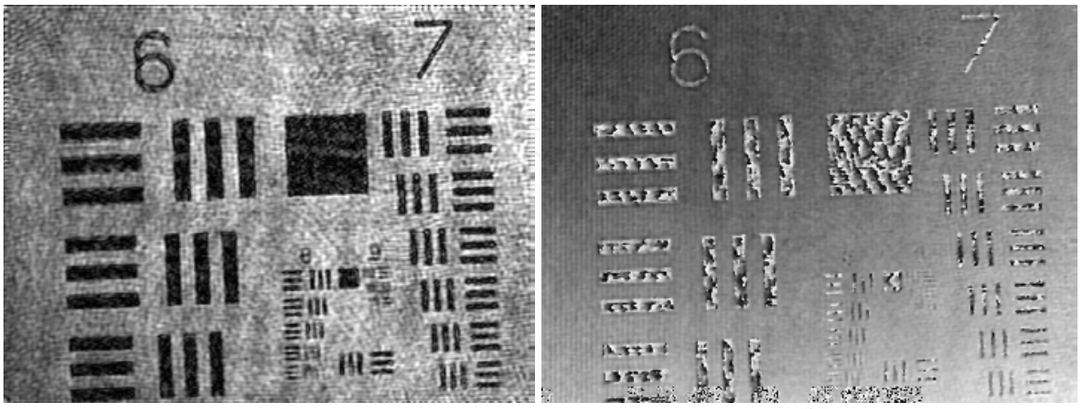

(a) (b)

Fig. 9. Reconstruction of the intensity image (a) and the phase image (b) at $z = D = 173\ mm$

Phase curvature compensation:

It should be noted from figure 9b that mixed phase images ϕ_o and ϕ_B appear, which are related with the phase of the objects and the quadratic constant phase factor S_ϕ respectively. Both phase images are shown more clearly in figure 10.

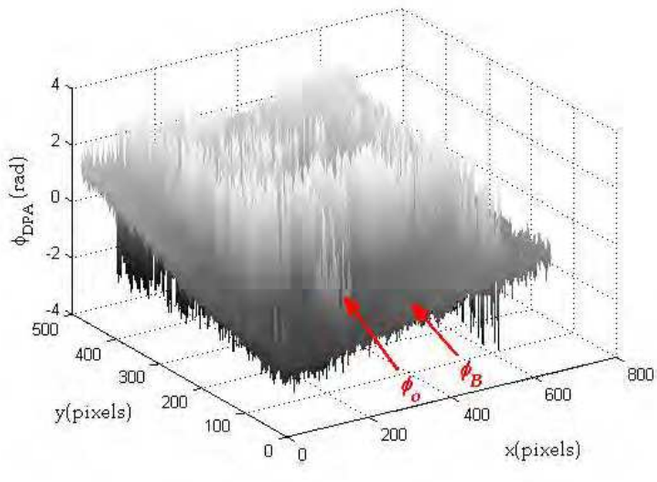

Fig. 10. Pseudo 3D rendering of the phase image ϕ_{DPA} presented in figure 9b.

Due to the slow variation of ϕ_B, it can be considered as a background contribution to the phase image of the objects ϕ_o, thus the problem of phase curvature compensation can be treated as a problem of phase image background subtraction. This way, alternative image background subtraction methods can be used. A procedure (Ankit & Rabinkin, 2007), that consists of applying a median filter with a large kernel size to the phase image represents a quick and simple way to obtain ϕ_B, figure 11.

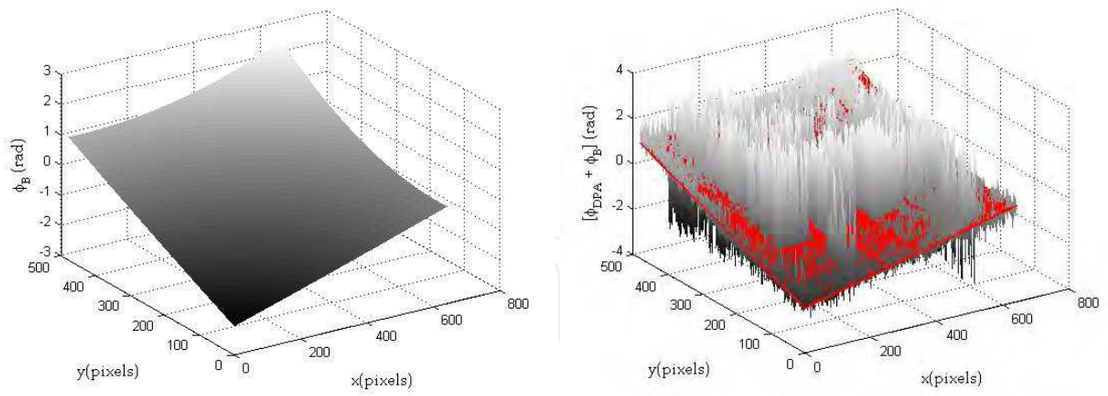

(a) (b)

Fig. 11. Pseudo 3D rendering of the phase image ϕ_B (a) and simultaneous visualization of ϕ_{DPA} and ϕ_B *(color red)* (b)

As can be appreciated from figure 11b, a good fitting of ϕ_B is achieved when a median filter with a large kernel size is applied over ϕ_{DPA}.

Taking into consideration that the reconstructed complex wavefield ψ_{DPA} can be expressed as the superposition of two contributions corresponding to the object wave front $exp(i\phi_o)$ and the spherical wave front $exp(i\phi_B)$,

$$\psi_{DPA}(x',y';d') \propto \exp(i\phi_o)\exp(i\phi_B) \tag{10}$$

then, the phase curvature can be compensated numerically by the calculation of the corrected phase image $\phi_{DPA}^{corr}(x',y';d')$,

$$\phi_{DPA}^{corr}(x',y';d') \cong \phi_o(x',y';d') = \arg\left[\psi_{DPA}(x',y';d')\exp(-i\phi_B)\right] \tag{11}$$

In figure (12a) is presented the corrected phase image calculated by Eq. (11).

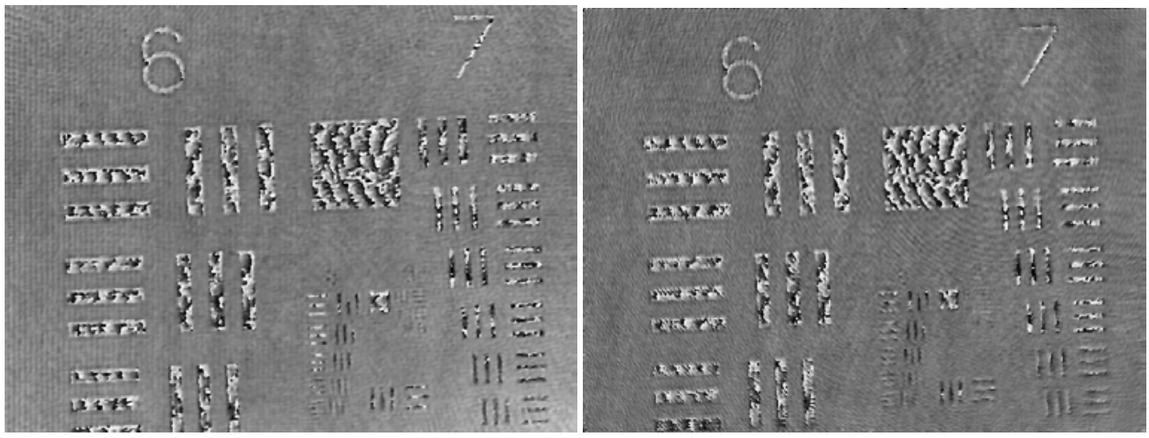

(a) (b)

Fig. 12. Corrected phase image $\phi_{DPA}^{corr}(x',y';d')$ (a). Phase image calculated with ASA, but using a reference hologram (b).

For comparison figure 12b shows the phase image calculated from the same hologram and reconstructed with the ASA, but using a reference hologram (Colomb et al., 2006).

3.1.4 Refocusing at different reconstruction distances

With the analysis of the intensity image reconstruction we demonstrate the ability of DPA to refocus at different distances *d'*.

Figure 13 shows a comparison between DPA (row A) and ASA (row B) in the reconstruction of several holograms where the best focus of the image is: *d'=0 mm*, *d'=10 mm*, *d'=30 mm* and *d'=70 mm*.

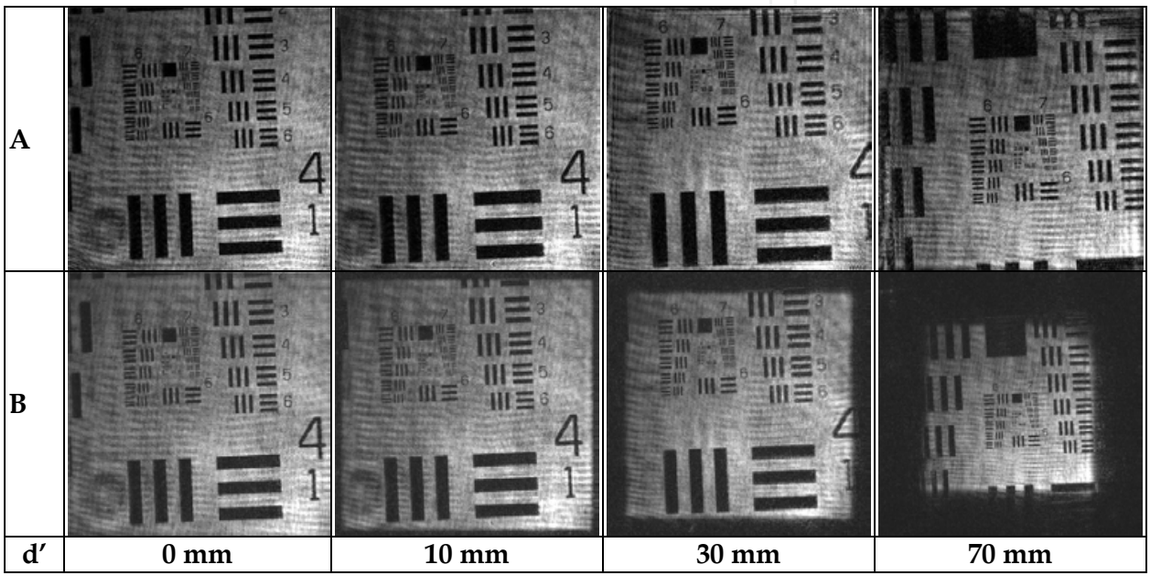

Fig. 13. Comparison between DPA (row A) and ASA (row B) in the intensity image reconstruction for different distances *d'*.

According to figure 13, as the reconstruction distance *d'* increases, the size of the reconstructed intensity image is constant for both algorithm until *d' = 10 mm*. For values of *d'* bigger than 20 mm, the size of the reconstructed intensity image is reduced when the ASA is used, whereas it remain constant when is used the DPA. The effect is most obvious for *d' = 70 mm*.

Summarizing, two main advantages can be attributed to the DPA algorithm: capability to maintain the size of a reconstructed image, independent of the reconstruction distance and wavelength for objects larger than a CCD and phase reconstruction with curvature compensation without the necessity of either a reference hologram or parameter adjustment. For a hologram of 1024 x 768 pixels using a standard PC computer (Pentium IV, 3.2 GHz) the required time for the calculation of the phase image, the intensity image and the distance *D* is 2.3, 1.2 and 2.6 seconds respectively. The limitations are related to the two manual filtering stages that exist in the reconstruction process. After the first propagation, the manual selection of Fourier transform components at the back focal plane can introduce others element that disturb the reconstructed plane.

4. Microscopic object analysis using DHM

In this section we study microscopic objects with regular forms starting from their Fraunhofer diffraction patterns obtained with DHM. Two types of analysis are considered: (i) analysis of objects according to their spatial distribution and (ii) analysis of individual objects.

4.1 Fourier transformation at the back focal plane

From Eq. (5) it can be seen that the wave field at the back focal plane õ*(u,v)* is proportional to the Fourier transform of the objects except for the spherical wave front $S_{\varphi'}$ which represents a quadratic phase curvature factor that causes a phase error if the optical Fourier transformation is computed (Poon, 2007).

Using DHM it is possible to find the exact Fourier Transform of objects at the back focal plane. The complex conjugate of the constant phase factor $S_{\phi}(u,v)$, can be expressed through the well-known parameters of the experimental design presented in figure 1, i.e. *d'*, *D* and *f*,

$$\tilde{S}_{\phi}(u,v) = \frac{i}{\lambda f}\exp\left[\frac{-ik}{2(D+d')}\left(u^2+v^2\right) - f\left(f+2\right)\right] \tag{12}$$

Multiplying Eq. (12) by Eq. (5), the constant phase factor is eliminated and the exact Fourier Transform at back focal plane $\Im_{BFP}$ is obtained,

$$\Im_{BFP}(u,v) = \psi^{f}_{SFTF}(u,v;z=D)\,\tilde{S}\phi(u,v) = \Im\left[o(x_o,y_o,\lambda f)\right] \tag{13}$$

Calculating the intensity distribution from Eq. (13), the object's Fraunhofer diffraction pattern $I_{FDP}(u,v)$ is obtained,

$$I_{FDP}(u,v) = \left|\Im_{BFP}(u,v)\right|^2 \tag{14}$$

Eq. (14) offers a powerful tool in microscopic analysis because the Fourier Transform plane can be manipulated and different techniques of Fourier optics can be applied digitally, such as pattern recognition, image processing and others.

4.2 System magnification

The knowledge of system magnification is important when quantitative relations between lineal dimensions of the enlarged image and the microscopic object have to be known. In DHM the total system magnification depends on where the camera CCD is placed.

The image and the back focal planes are related by a Fourier transformation, thus lineal distance in the image plane can be extracted by the reciprocal of the corresponding lineal distance in the focal plane. In the working conditions with the capture of one hologram, figure 14a, the Fraunhofer pattern is reconstructed, figure 14b. A micrometric scale *Mitutoyo®* with 100 lines per mm was used as object.

The magnification of the system $M_T = d_i/d_o$ can be determined by the relation between two distances d_i and d_o in the image and object plane respectively. We determine the distance $d_i = 0.89\ mm$ between two bar in the image plane as the reciprocal value of the measured distance $d_f = 1.12\ mm$ between two contiguous diffraction points on the Fraunhofer pattern.

This method for determining d_i is more accurate that their direct measure over the image plane. With the knowledge that the distance between the two bar in the object plane is d_o = *10 μm*, M_T = *0.89/0.010 = 89*.

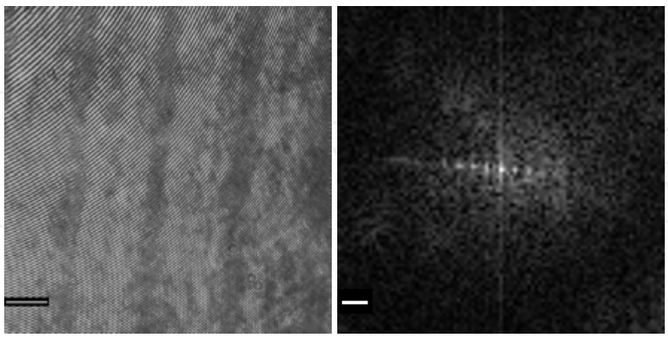

(a) (b)

Fig. 14. Digital hologram, scale bar 445 μm (a), Fraunhofer pattern, scale bar 2 mm^{-1} (b)

4.3 Analysis of objects according to their distribution

We consider objects with regular forms and two different forms of spatial distribution: randomly and periodically distributed. The objects' parameters can be determined by diffraction pattern manipulation in a simple and accurate way. This is an example of objects analysis that is important to biological and materials sciences.

4.3.1 Similar objects in random arrangement

We consider a sample of mouse blood cell as an example of random distribution of similar objects and use the proposed methodology to determine the diameter of cells. Figure 15a shows the hologram recorded with the experimental set-up.

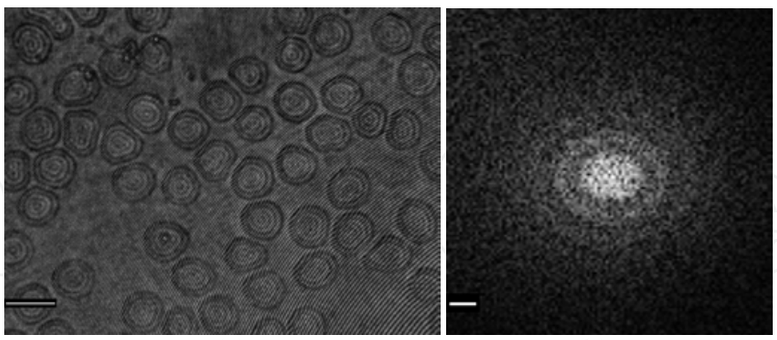

(a) (b)

Fig. 15. Digital hologram (a), Fraunhofer pattern, scale bar *2* mm^{-1} (b).

Applying Eq. (14) the Fraunhofer pattern is obtained, figure 15b. As predicted by theory, the Fraunhofer diffraction pattern has a 'spotty' interference pattern, with a central peak and intensity in the diffraction plane that shows random fluctuations on a general background.

The radial intensity distribution $I_R(r)$, figure 16-upper, is measured by scanning the Fraunhofer diffraction pattern along radial lines (Palacios et al., 2001).

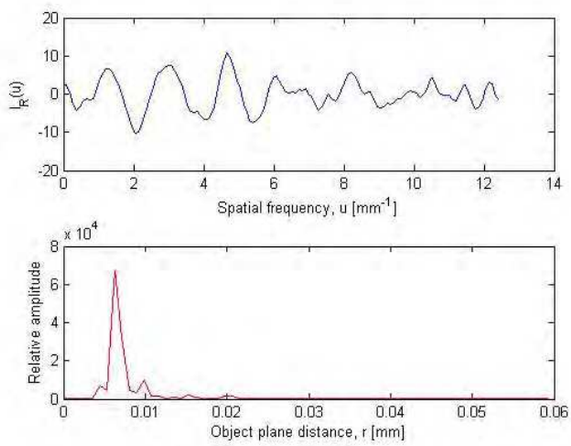

Fig. 16. Upper- the radial intensity curve $I_R(r)$, lower- spectrum of $I_R(r)$.

For each r value the intensity $I_R(r)$ is the result of averaging the intensity values $I_{FDP}(u,v)$ along the circumference from 0^o to 360^o, mathematically this operation can be represented by the expression,

$$I_R(r) = r^3 \frac{\sum_{\theta=1}^{360} I\left(x' = C_x(r,\theta), y' = C_y(r,\theta), d' = D\right)}{360} \tag{15}$$

where, $C_x(r,\theta) = N/2 + r\cos\theta$, $C_y(r,\theta) = N/2 - r\sin\theta$, with $0^o < \theta \leq 360^o$ and $0<r\leq N/2$.
The spatial coordinates in the Fraunhofer diffraction pattern are defined on basis of the Fraunhofer diffraction pattern pixel resolution Δu, which is determined directly from the Fresnel diffraction formula at the reconstruction distance $z = D$. In this way, the radial distance $u=j\Delta u$, $j=0,1,\ldots,Np$, where Np is the points number of the radial intensity curve and $\Delta u = \lambda D/M\Delta\xi$. In the frequency spectrum, the spatial frequency is $f_u=j/Np\Delta u$, $j=0,1,..Np$.
The spectral analysis of the radial intensity curve $I_R(r)$ is carried out by the calculation of the square of the modulus of its 1D Fourier transform. In the resulting spectrum, figure 16-lower, the harmonic components are seen. As seen, only one fundamental harmonic that characterizes the diameter ($r_o = 6.3\ \mu m$) of the mouse blood cell appears.

4.3.2 Similar objects in periodical arrangement

In this section we consider a sample of periodically hexagonal structures inscribed on a plastic material with an ion beam as an example of regularly repeated identical objects.
In figure 17 is shown the hologram and intensity image reconstruction with the parameters for a hexagonal real space lattice.
In the reconstructed intensity image the parameters for the hexagonal real space lattice on the image plane are shown: diffraction angle for hexagonal crystal $\gamma = 120^o$ and the unit cell parameters a, b which for hexagonal crystal meet the condition, $a = b$.
The Fraunhofer diffraction pattern is calculated and shown in figure 18a. In figure 18b a section of the reciprocal lattice is specified and drawn through the diffraction points, the parameters a^*, b^* and γ^* are shown.

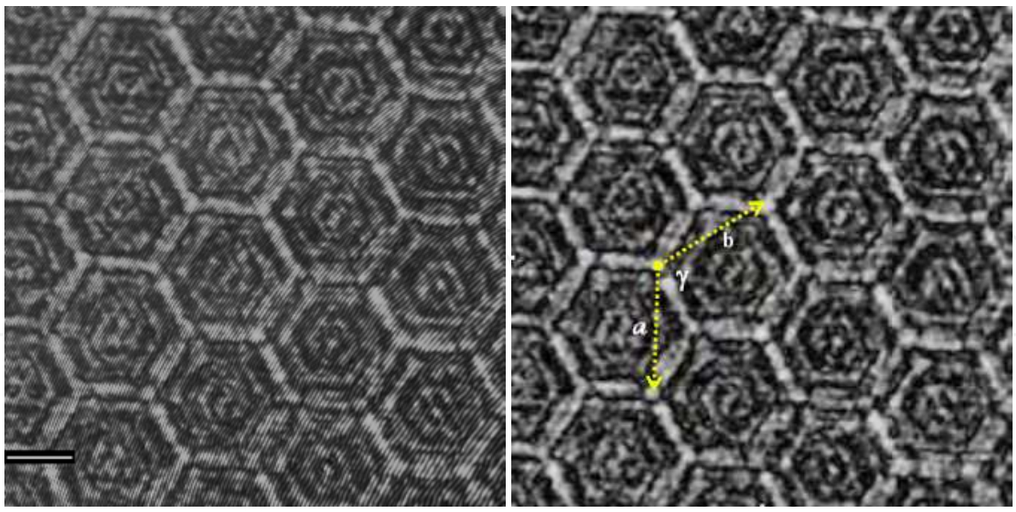

(a) (b)

Fig. 17. Digital hologram (a) and intensity image (b) of the sample. Scale bar *5μm*

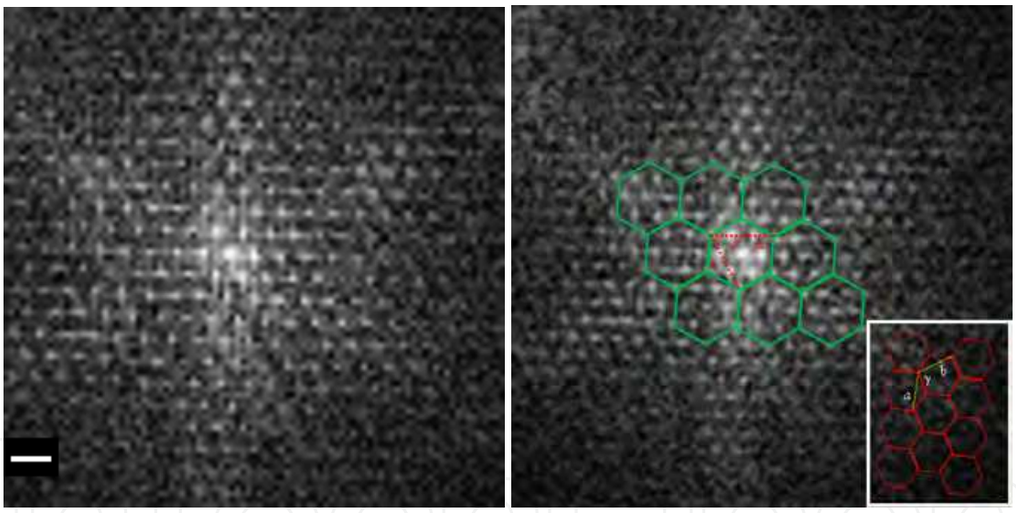

(a) (b)

Fig. 18. Fraunhofer diffraction pattern (a), scale bar 2 mm^{-1}. Over diffraction pattern it is drawn the reciprocal lattice (b). (*Inset: Representation of the real space*)

As shown in figure 18b, according to the theory of crystal diffraction, the reciprocal lattice edges of dimensions a^* and b^* are respectively perpendicular to the cell edges b and a, and quantities are related by the following expressions,

$$a^* = \frac{K}{a \sin \gamma^*} \quad b^* = \frac{K}{b \sin \gamma^*} \quad \text{and} \quad \gamma^* = 180^o - \gamma \tag{16}$$

where $K = \lambda L$ is the constant of diffraction, where λ the wavelength of monochromatic radiation and L is the camera length, i.e., the distance from the specimen to the diffraction

plane. Applying the relations (16) the diffraction angle in the reciprocal lattice $\gamma^* = 60^o$ is determined and by measuring the parameters $a^* = b^* = 1.15\ mm$ in the reciprocal lattice the parameters $a' = b' = 863\ \mu m$ are calculated. It can be noticed that a' and b' are the real lattice parameters, but in the image plane. The parameters a, b of real lattice in the object plane are obtained dividing a' and b' by the total system magnification $M_T = 89$, i.e., $a = b = a'/M_T = b'/M_T = 9.69\ \mu m$. This value coincides with that obtained by AFM.

4.4 Calculation of nucleated cell dimensions

We demonstrate in this section the potentialities of Digital Holographic Microscopy in the determination of morphological parameters of nucleated cells. The spectral analysis of the radial behaviour of the Fraunhofer diffraction pattern allows the correlation between the peaks observed in the spectra and lineal dimensions of the cell.

As an example of application a sample of oral mucosa epithelial cell was selected. These cells have a nucleus inside a regular cytoplasm, figure 19.

Fig. 19. Oral mucosa epithelial cell, optical microscopy image. Scale bar $20\ \mu m$

Two cases were analyzed, (i) the nucleus of the cell is located approximately at the centre of the cell and (ii) the nucleus is outside the centre.

Figure 20 shows the hologram (left) and the phase image reconstruction (right) of cell with the nucleus at the centre (A) and outside of centre (B). Both holograms were captured with the apparatus of figure 1 and the phase image was obtained by the calculation of the argument of Eq. (9) with $d' = 0$.

For both holograms the Fraunhofer pattern was calculated and is shown in figure 21 (left). Applying the spectral analysis of the Fraunhofer pattern radial intensity, the corresponding frequency spectra are obtained, figure 21 (right). In each spectrum a sequence of peaks are seen. In the case of cell with nucleus at the centre (A) four peaks appear in the spectrum, which is different for the case of the cell with nucleus outside the centre (B) where six peaks are observed in the spectrum.

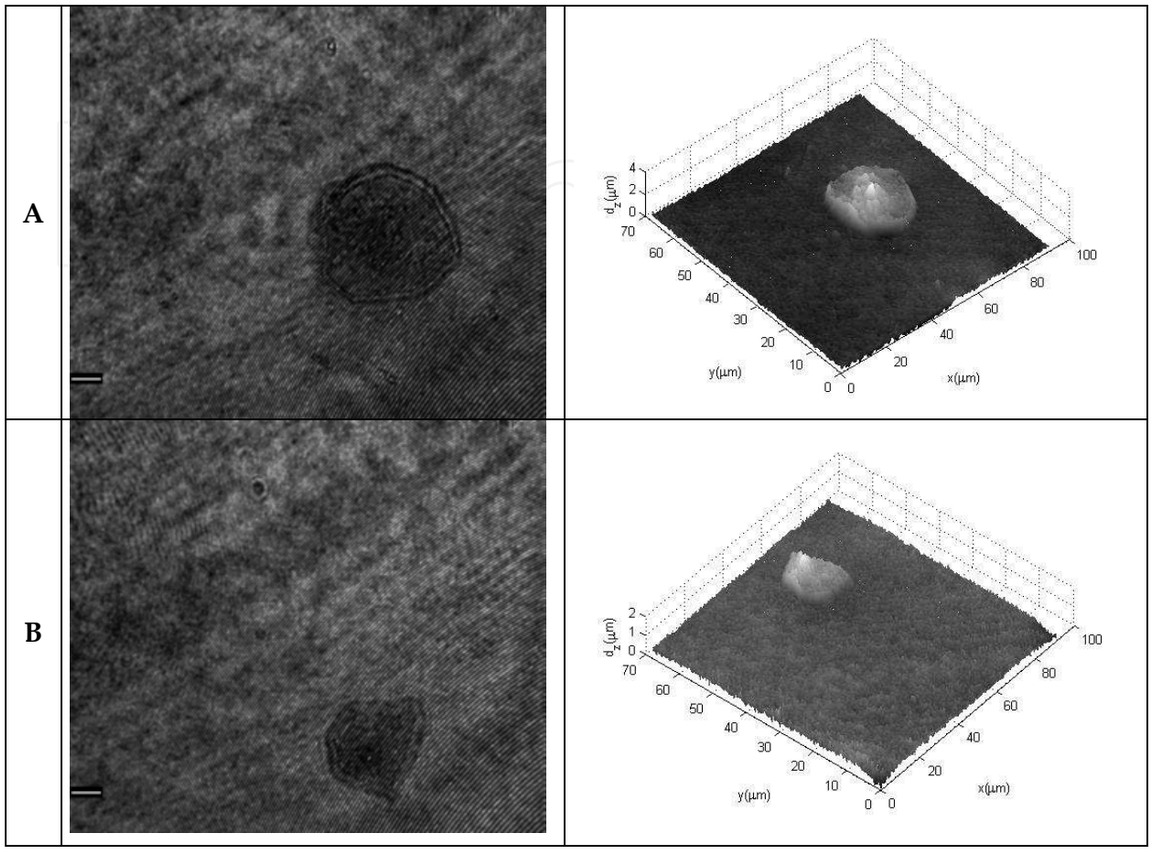

Fig. 20. Hologram (left) and phase image reconstruction (right) of cell with the nucleus at the centre (A) and outside of centre (B). Scale bar *20 μm*

The correlation between the peaks observed in the spectra and the diameter of cytoplasm and nucleus as well as other dimensions of the cell is definite, i.e., the peak position in the spectra is related with a lineal dimension in the cell.

In the case of the cell with the nucleus at the centre the peaks mean: peak (1) is characteristic of the nucleus diameter Dn, peak (2) characterizes half of the difference of both diameters, (Dc-Dn)/2, peak (3) characterizes half of the sum of both diameters, (Dc+Dn)/2 and peak (4) is characteristic of the cytoplasm diameter Dc.

If we consider the case of a cell with eccentric nucleus, which is shifted a distance *e* from the centre of cytoplasm two peaks correspond to the nuclear and cytoplasm diameters, (1) and (6) respectively, and the other four to half of the sums and differences of these two plus/minus the eccentricity 'e': peak (2) → (Dc-Dn)/2 – e, peak (3) → (Dc+Dn)/2 – e, peak (4) → (Dc-Dn)/2 + e, peak (5) → (Dc+Dn)/2 + e. The equivalent intervals in the cell are shown in figure 22.

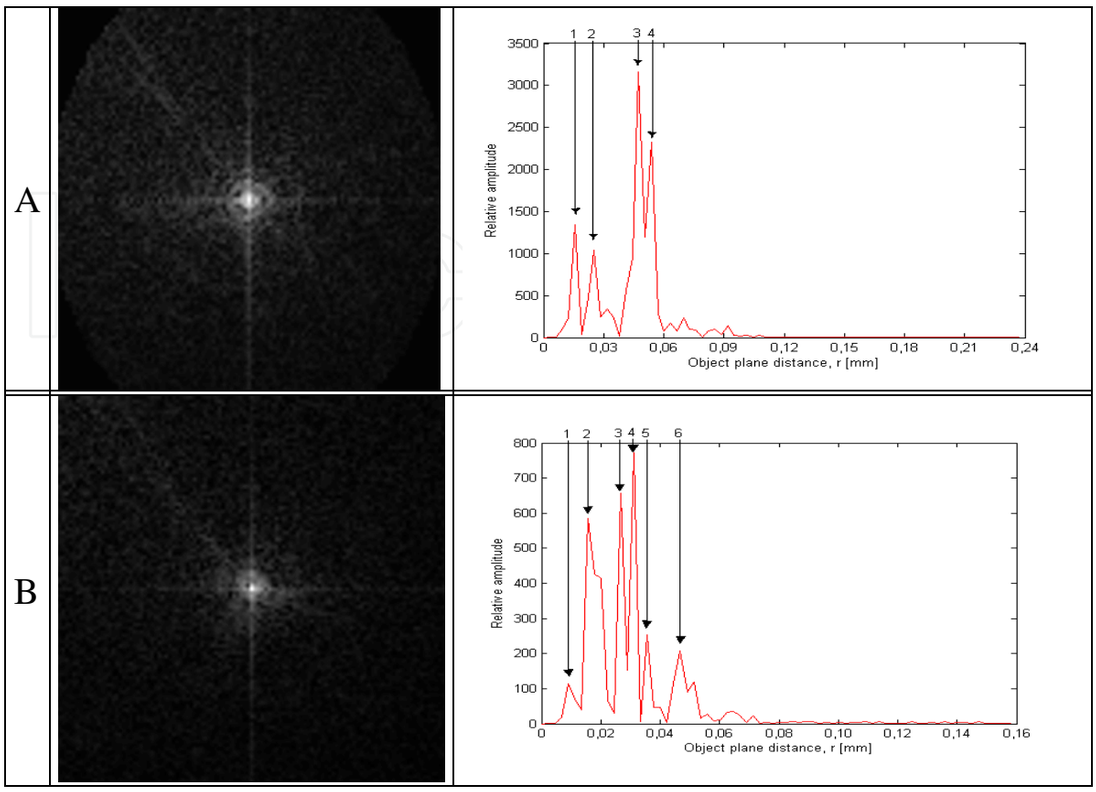

Fig. 21. Fraunhofer pattern (left) and the corresponding spectrum of their radial intensity (right) of cell with the nucleus at the centre (A) and outside of centre (B).

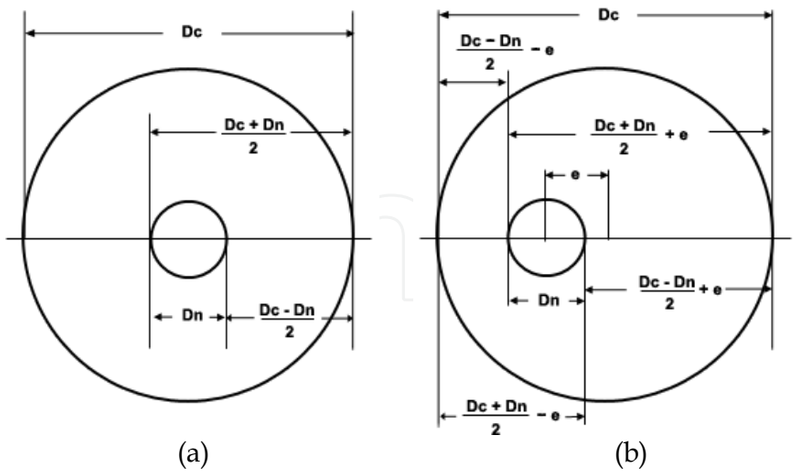

(a) (b)

Fig. 22. Cellular dimensions reflected in the diffraction patterns: diagram (a) and (b) correspond to lineal dimensions of spectrums represented in figure 21 (right).

These results agree with theoretical predictions and experimental test presented in (Türke et al., 1978), although with the proposed method simpler the recording process and data processing are simpler.

4.5 Object detection

In this section we demonstrate that object detection is another example of objects analysis that can be realized by the examination of Fraunhofer diffraction patterns obtained by DHM.

The hologram of a microscopic character with the shape of a zero '0', figure 23a, is used to calculate the phase image shown in figure 23b.

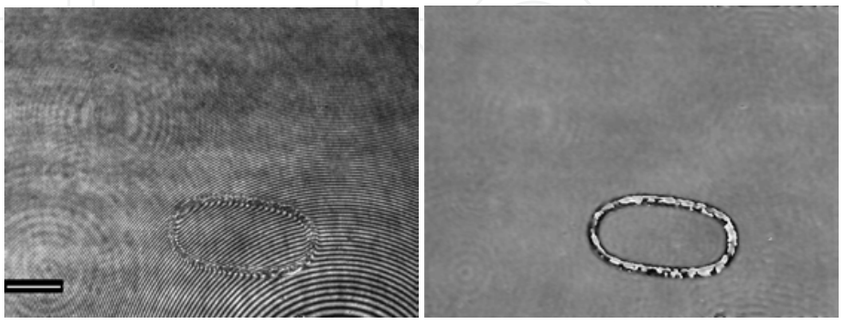

(a) (b)

Fig. 23. Hologram of a microscopic character with zero shape (a), scale bar: *50 μm*. Phase image reconstruction (b)

The microscopic character with zero shape will be detected when mixed with other microscopic characters. Figure 24 shows two holograms and the respective phase image reconstructions corresponding to microscopic characters with two different shapes: twenty '20' (A) and ten '10' (B). Here besides the microscopic character other elements exist to complicate the detection process.

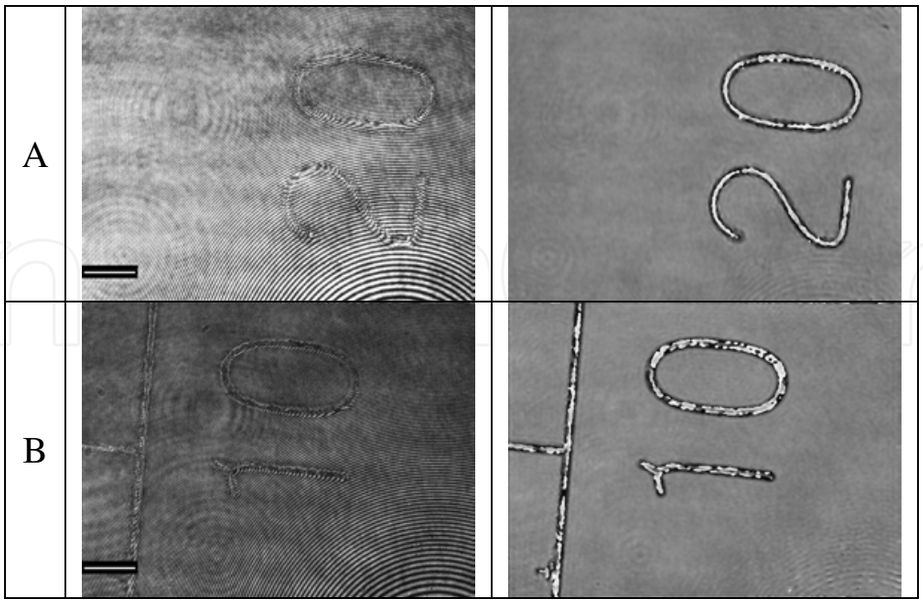

Fig. 24. Holograms, scale bar: *50 μm* (left) and phase image reconstruction (right) corresponding to microscopic characters with two different shapes: twenty '20' (A) and ten '10' (B).

The hologram of a microscopic character with zero shape, figure 23a, is used to calculate the Fraunhofer diffraction pattern shown in figure 25a. The radial intensity curve $I_R(u)$ and the corresponding frequency spectrum are shown in figure 25b.

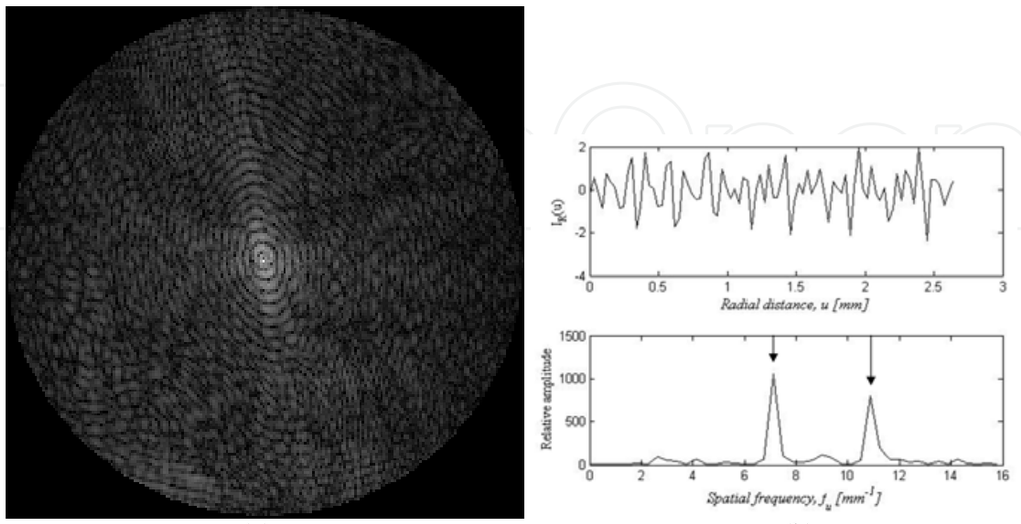

(a) (b)

Fig. 25. Fraunhofer diffraction pattern of the microscopic character with zero shape (a) and the radial intensity curve (b)-upper and the corresponding frequency spectrum (b)-lower.

According to figure 25a, the Fraunhofer diffraction pattern consists of elliptically shaped fringes with similar forms to that of the zero character. The fringes' width variation along their perimeter is detected by the radial intensity curve and with the subsequent spectral analysis the largest and smallest radius of the zero character can be obtained. The two peaks are signaled with arrows in the spectrum, figure 25b-down. They are positioned at the spatial frequencies $7.12\ mm^{-1}$ and $11.10\ mm^{-1}$, that represent the biggest and smallest radius of the zero character respectively. According to the peaks' spatial frequencies, the largest and the smallest radii are $140\ \mu m$ and $90\ \mu m$ respectively.

For object detection the holograms of a microscopic characters with '20' and '10' shapes, figure 24 (left), were used to calculate the Fraunhofer diffraction patterns shown in figure 26 (left). The radial intensity curve $I_R(u)$ and the corresponding frequency spectrum is shown in figure 26 (right).

In the frequency spectrum shown in figure 26 (right) appear, mixed with other peaks, two peaks at the same spatial frequency as those that are characteristic of the zero shape frequency spectrum. In this way, the object detection can be generalized for other objects with irregular forms, because the spectrum of the radial curve of the object's diffraction pattern presents a sequence of peaks that characterize the form of the object. A unique spectrum is associated with each form.

As has been shown, this method of object detection is similar to the qualitative analysis in x-ray diffraction, i.e. the presence of an object is characterized by the presence of peaks in appropriate positions in the spectrum. This analogy is very important because all the developed tools for the qualitative analysis in x-rays can be used for object detection.

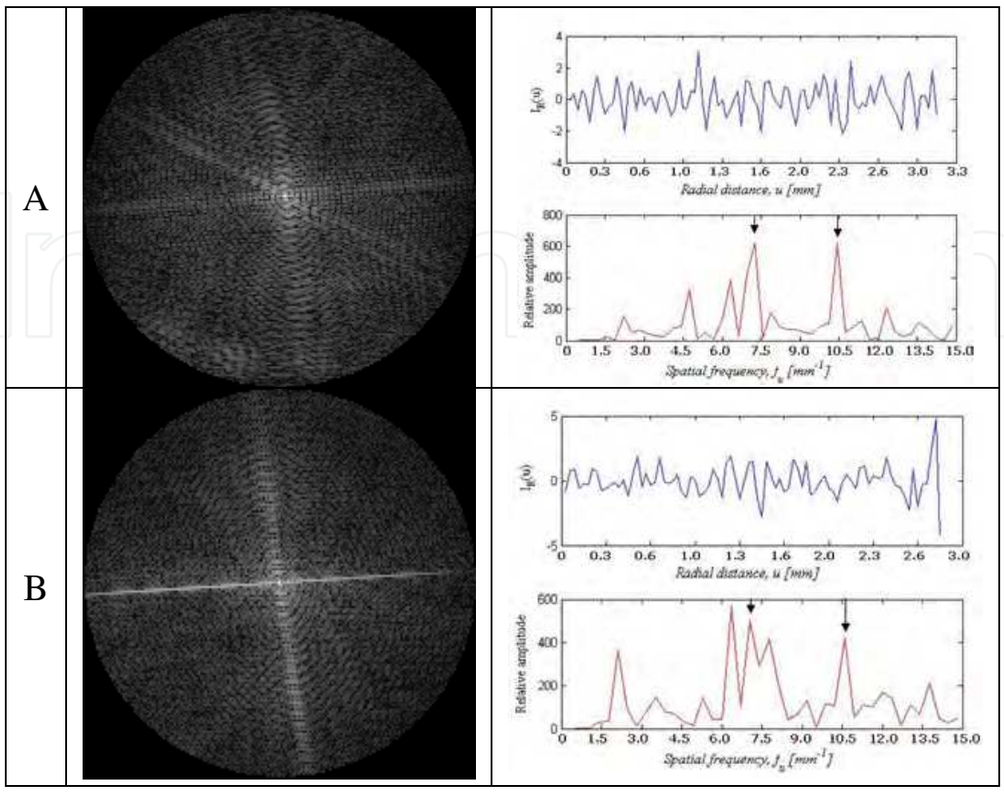

Fig. 26. Fraunhofer diffraction patterns of corresponding hologram of figure 24 (left) and the radial intensity curve with the corresponding frequency spectrum (right).

5. Conclusion

In this chapter, an alternative methodology for image reconstruction and object analysis in digital holographic microscopy is discussed. The model we use for image reconstruction is specific for digital holographic microscopy; it includes a first propagation from the hologram plane to obtain the Fourier Transform plane of the object at the back focal plane of the microscope objective lens and then a second propagation is applied to find out the image wave field at the reconstruction plane. Using digital hologram reconstruction as a method for calculating the amplitude and intensities distributions of the optical field on the Fourier Transform plane microscopic objects with regular forms are studied. Random and periodical distributions of objects are considered. The lineal dimensions of the objects are determined by manipulating the diffraction pattern in a simple and accurate way. The advantages of this methodology are summarized as follows: (a) using a single hologram the phase image is calculated with simple operation for phase curvature correction, (b) there are no limitations in the minimum reconstruction distance, (c) capability to maintain the size of a reconstructed image, independent of the reconstruction distance and wavelength for objects larger than a CCD, and (d) the spectral analysis of the radial intensity curve of the Fraunhofer diffraction pattern allows the determination of the lineal dimensions of the objects.

6. Acknowledgment

This work is supported by the Brazilian research agencies FAPESP and CAPES, University of Oriente, Cuba and the National University of Colombia.

7. References

Ankit, K. & Rabinkin, D. (2007). Edited by Luk, Franklin T. Proceedings of the SPIE, Volume 6697, pp. 66970E-66970E-17.

Colomb, T.; Kühn, J.; Charrière, F.; Depeursinge, C.; Marquet, P. & Aspert, N.(2006). Opt. Express 14, 4300.

Cuche, E.; Marquet, P. & Depeursinge, C. (1999). Appl. Opt. 38, 6994–7001.

Cuche, E.; Marquet, P. & Depeursinge, C. (2000). Appl. Opt. 39, 4070–4075.

De Nicola, S.; Finizio, A.; Pierattini, G.; Ferraro, P. & Alfieri, D. (2005). Opt. Express 13, 9935–9940.

Demetrakopoulos, TH.; Mittra, R. (1974). Appl Opt., 13:665-670.

Ferraro, P.; Nicola, S. D.; Finizio, A.; Coppola, G.; Grilli, S.; Magro, C. & Pierattini, G. (2003). Appl. Opt. 42, 1938–1946.

Goodman, J. W. (1968). McGraw-Hill, San Francisco, Calif.

Grilli, S.; Ferraro, P.; Nicola, S. D.; Finizio, A.; Pierattini, G. & Meucci, R. (2001). Opt. Express 9, 294–302.

Kreis, T.; Adams, M. & Jüptner, W. (1997). Proc. SPIE 3098, 224.

Lim, J. S. (1990). Englewood Cliffs, NJ, Prentice Hall, pp. 218-237.

Lipson, S. G. & Lipson, H. (1981) Second edition. Cambridge University Press.

Miccio, L.; Alfieri, D.; Grilli, S.; Ferraro, P.; Finizio, A.; Petrocellis, L. D. & Nicola S. D. (2007). Appl Phys. Lett. 90, 041104-1.

Murata, S. & Yasuda, N. (2000). Opt. Laser Technol. 32, pp. 567.

Palacios, D.; Palacios, F.; Sajo-Bohus, L. & Pálfalvi, J. (2001). J. Rad. Meas. 34, pp. 119-122.

Palacios, F.; Palacios, D.; Palacios, G.; Gonçalves, E.; Valin, J.; Sajo-Bohus, L. & Ricardo, J. (2008). J. Opt. Comm., Vol. 281, Issue 4, 15, pp 550-558.

Palacios, F.; Ricardo, J.; Palacios, D.; Gonçalves, E.; Valin, J. & De Souza, R. (2005) Opt. Comm. Vol. 248/1-3, pp 41-50.

Pan, G. & Meng, H. (2003). Appl. Opt. 42, 827.

Pedrini, G.; Schedin, S. & Tiziani, H. J. (2001). J. Mod. Opt. 48, 1035–1041.

Poon, T.C. (2007). *Optical Scanning Holography with Matlab®*, Springer Science+Business Media, LLC.

Schedin, S.; Pedrini, G.; Tiziani, H.; Aggarwal, A. & Gusev, M. (2001), Appl. Opt. 40, pp. 100.

Schilling, B.W.; Poon, T.C.; Indebetouw G.; Storrie B.; Shinoda K.; Suzuki Y. & Wu M.H. (1997). Opt. Lett. 22, pp. 1506-1508.

Schnars, U. (1994). J. Opt. Soc. Am. A 11, 2011.

Stadelmaier, A. & Massig, J. H. (2000). Opt. Lett. 25, 1630–1632.

Takaki, U. & Ohzu, H. (1999). Appl. Opt. 38, pp. 2204.

Türke, B.; Seger, G.; Achatz M. & Seelen W. (1978). App. Opt. 17:2754-2761.

VanLigten, R. F. & Osterberg, H. (1966). Nature, 211, pp. 282-283.

Wagner, C.; Osten, W. & Seebacher, S. (2000). Opt. Eng. 39, pp. 79.

Yamaguchi, I.; Matsumura, T. & Kato, J. (2002) Opt. Lett. 27, 1108.

Yaroslavsky, L. & Merzyalov, N. (1980), Consultants Bureau.

Yu, L. & Kim, M.K. (2005). Opt Lett 2005, 30:2092.
Yu, L.; Mohanty, S.; Zhang, J.; Genc, S.; Kim, M.K.; Berns, M.W. & Chen, Z. (2009) Opt. Express, Vol 17, No. 14.
Zhang, F.; Yamaguchi, I. & Yaroslavsky, L. P. (2004). Opt. Letters, Vol. 29, No. 14.

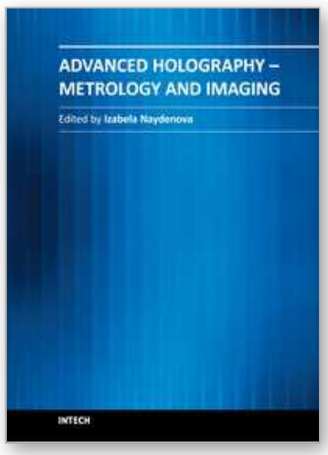

Advanced Holography - Metrology and Imaging

Edited by Dr Izabela Naydenova

ISBN 978-953-307-729-1
Hard cover, 374 pages
Publisher InTech
Published online 09, November, 2011
Published in print edition November, 2011

Advanced Holography - Metrology and Imaging covers digital holographic microscopy and interferometry, including interferometry in the infra red. Other topics include synthetic imaging, the use of reflective spatial light modulators for writing dynamic holograms and image display using holographic screens. Holography is discussed as a vehicle for artistic expression and the use of software for the acquisition of skills in optics and holography is also presented. Each chapter provides a comprehensive introduction to a specific topic, with a survey of developments to date.

How to reference

In order to correctly reference this scholarly work, feel free to copy and paste the following:

Francisco Palacios, Oneida Font, Jorge Ricardo, Guillermo Palacios, Mikiya Muramatsu, Diogo Soga, Daniel Palacios, José Valin and Freddy Monroy (2011). Alternative Reconstruction Method and Object Analysis in Digital Holographic Microscopy, Advanced Holography - Metrology and Imaging, Dr Izabela Naydenova (Ed.), ISBN: 978-953-307-729-1, InTech, Available from: http://www.intechopen.com/books/advanced-holography-metrology-and-imaging/alternative-reconstruction-method-and-object-analysis-in-digital-holographic-microscopy

INTECH
open science | open minds

InTech Europe
University Campus STeP Ri
Slavka Krautzeka 83/A
51000 Rijeka, Croatia
Phone: +385 (51) 770 447
Fax: +385 (51) 686 166
www.intechopen.com

InTech China
Unit 405, Office Block, Hotel Equatorial Shanghai
No.65, Yan An Road (West), Shanghai, 200040, China
中国上海市延安西路65号上海国际贵都大饭店办公楼405单元
Phone: +86-21-62489820
Fax: +86-21-62489821

IntechOpen